PCCP

PAPER

View Article Online
View Journal | View Issue

Cite this: *Phys. Chem. Chem. Phys.*, 2016, **18**, 10727

A comprehensive comparison of dye-sensitized NiO photocathodes for solar energy conversion†

Christopher J. Wood,‡[a] Gareth H. Summers,‡[a] Charlotte A. Clark,[a] Nicolas Kaeffer,[b] Maximilian Braeutigam,[cd] Lea Roberta Carbone,[e] Luca D'Amario,[f] Ke Fan,[g] Yoann Farré,[h] Stéphanie Narbey,[i] Frédéric Oswald,[i] Lee A. Stevens,[j] Christopher D. J. Parmenter,[k] Michael W. Fay,[k] Alessandro La Torre,[k] Colin E. Snape,[l] Benjamin Dietzek,[cd] Danilo Dini,[e] Leif Hammarström,[f] Yann Pellegrin,[h] Fabrice Odobel,[h] Licheng Sun,[g] Vincent Artero[b] and Elizabeth A. Gibson‡*[a]

Received 6th September 2015,
Accepted 21st December 2015

DOI: 10.1039/c5cp05326a

www.rsc.org/pccp

We investigated a range of different mesoporous NiO electrodes prepared by different research groups and private firms in Europe to determine the parameters which influence good quality photoelectrochemical devices. This benchmarking study aims to solve some of the discrepancies in the literature regarding the performance of p-DSCs due to differences in the quality of the device fabrication. The information obtained will lay the foundation for future photocatalytic systems based on sensitized NiO so that new dyes and catalysts can be tested with a standardized material. The textural and electrochemical properties of the semiconducting material are key to the performance of photocathodes. We found that both commercial and non-commercial NiO gave promising solar cell and water-splitting devices. The NiO samples which had the two highest solar cell efficiency (0.145% and 0.089%) also gave the best overall theoretical H_2 conversion.

Introduction

Since He *et al.* reported the first dye-sensitized NiO photocathode and assembled it in a tandem dye-sensitized solar cell, an opportunity to increase the efficiency of solar energy conversion in photoelectrochemical devices has been recognised.[1,2] Firstly, the theoretical maximum efficiency of dye-sensitized solar cells (DSCs) is increased from 33% to 43% by replacing the platinized counter electrode in conventional DSC with a photocathode such as dye-sensitized NiO (Fig. 1a). Secondly, the redox electrolyte which completes the circuit in a photoelectrochemical solar cell (*i.e.* a DSC) can be replaced with water so that hydrogen can be generated at the photocathode and oxygen can be formed at the photoanode (Fig. 1b). This dye-sensitized photoelectrosynthetic cell (DPEC)[3] can produce hydrogen as a solar fuel while avoiding the requirement for sacrificial agents which are usually required in photocatalytic approaches.[3–5] In such architectures, catalysts, either molecular or materials, are usually required to facilitate water splitting into hydrogen and oxygen. Both types of device are relatively new concepts and the efficiency of the devices that have been reported is very low (2.42% efficiency for a tandem DSC[6] compared to 13% efficiency for the state of the art TiO_2-based DSCs;[7] maximum incident photon-to-current efficiencies up to 15% in TiO_2-based DPECs[8] compared to 0.6% for NiO-based DPECs[9]). Therefore the

[a] *School of Chemistry, The University of Nottingham, University Park, Nottingham, NG7 2RD, UK*
[b] *Laboratoire de Chimie et Biologie des Métaux, Université Grenoble Alpes, CEA, CNRS, 17 rue des Martyrs, 38000 Grenoble, France*
[c] *Institute of Photonic Technology (IPHT) Jena e. V., Albert-Einstein-Straße 9, D-07745 Jena, Germany*
[d] *Institute for Physical Chemistry and Abbe Center of Photonics, Friedrich-Schiller University Jena, Helmholtzweg 4, D-07743 Jena, Germany*
[e] *Department of Chemistry, University of Rome "La Sapienza", Rome, Italy*
[f] *Department of Chemistry-Ångström, Uppsala University, Box 259, SE-751 05 Uppsala, Sweden*
[g] *School of Chemical Science and Engineering, Royal Institute of Technology (KTH), 100 44 Stockholm, Sweden*
[h] *CEISAM, Chimie et Interdisciplinarité, Synthèse, Analyse, Modélisation, CNRS, UMR 6230, Faculté des Sciences et des Techniques Université de Nantes, 2, rue de la Houssinière, BP 92208, 44322 NANTES Cedex 3, France*
[i] *Solaronix, rue de l'Ouriette 129, CH-1170 Aubonne, Switzerland*
[j] *Division of Materials, Mechanics and Structures, Faculty of Engineering, University of Nottingham, University Park, Nottingham, NG7 2RD, UK*
[k] *Nottingham Nanotechnology and Nanoscience Centre, University of Nottingham, University Park, Nottingham, NG7 2RD, UK*
[l] *Department of Chemical and Environmental Engineering, Faculty of Engineering, University of Nottingham, University Park, Nottingham, NG7 2RD, UK*
† Electronic supplementary information (ESI) available. See DOI: 10.1039/c5cp05326a
‡ Present address: School of Chemistry, Newcastle University, Newcastle upon Tyne, NE1 7RU, UK. E-mail: Elizabeth.gibson@ncl.ac.uk

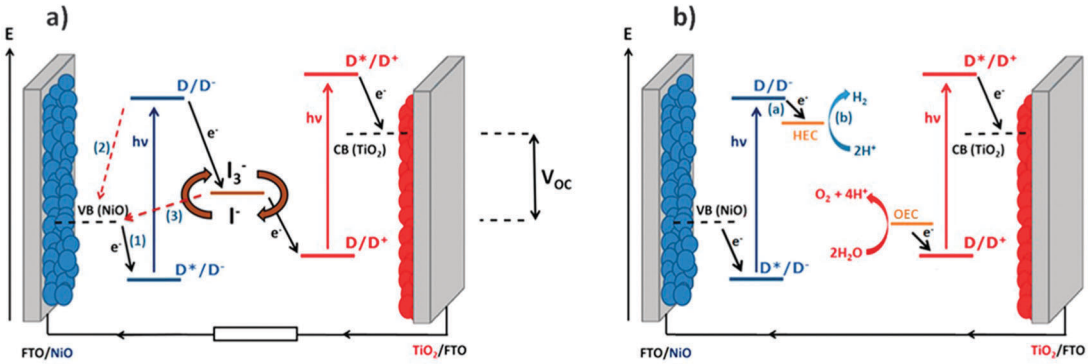

Fig. 1 Schematic illustration of (a) a tandem dye-sensitized solar cell and (b) a dye-sensitized photoelectrosynthetic cell. (VB: valence band; CB: conduction band; HEC: hydrogen evolution catalyst; OEC: oxygen evolution catalyst).

efficiency of tandem photoelectrochemical devices is limited by the performance of the photocathode. A breakthrough in this area is anticipated if highly efficient p-type photocathodes can be realised.[10]

Recently, the performance of NiO-based DSCs were reviewed in the context of the preparation method used for the mesoporous electrode.[11] It was observed that surface morphology is of primary importance to control the oxidation properties of NiO. The presence of defects is important to the performance of the device, especially the recombination reactions (2) and (3) in Fig. 1(a). The most efficient devices that have been reported were prepared from pre-formed NiO nanoparticles and companies such as Solaronix and Dyenamo are now selling screen-printable pastes. However, it is difficult to assess from the literature whether the source of NiO is important compared to other factors such as the device assembly method, choice of dye and sensitization conditions *etc.* we took the opportunity of the COST Action CM1202 on Supramolecular water splitting to organise a workshop for the benchmarking of different NiO electrodes, prepared in different research groups in Europe from lab-made or commercial sources, in DSCs and DPECs under the same conditions. This was designed to answer questions such as whether the control over the purity and crystallinity achieved by preparing the particles in house is preferential to purchasing NiO nanoparticles or commercial paste; whether the trends observed in DSCs can be translated directly to the performance of water-splitting DPECs.

The experiments were chosen so that the chemical-physical properties such as crystal size, BET surface area and electrochemical properties could be compared to the DSC and DPEC device performance. The dye **P1** (Fig. 2) was chosen because it has been used in both p-type DSCs and DPECs.[12,13] The I_3^-/I^- electrolyte for the DSCs was chosen because this redox couple is known to be optimised for this dye.[14] The $[Co(dmgBF_2)_2(H_2O)_2]$ (dmg^{2-}: dimethylglyoximato dianion) hydrogen evolving catalyst was chosen for the DPEC because it has been extensively characterised elsewhere and because Li *et al.* demonstrated that it can be incorporated into a **P1**-sensitized NiO DPEC to reduce protons.[8,15] In the devices, absorption of visible light by **P1** leads to electron transfer from NiO to the dye. The potential of

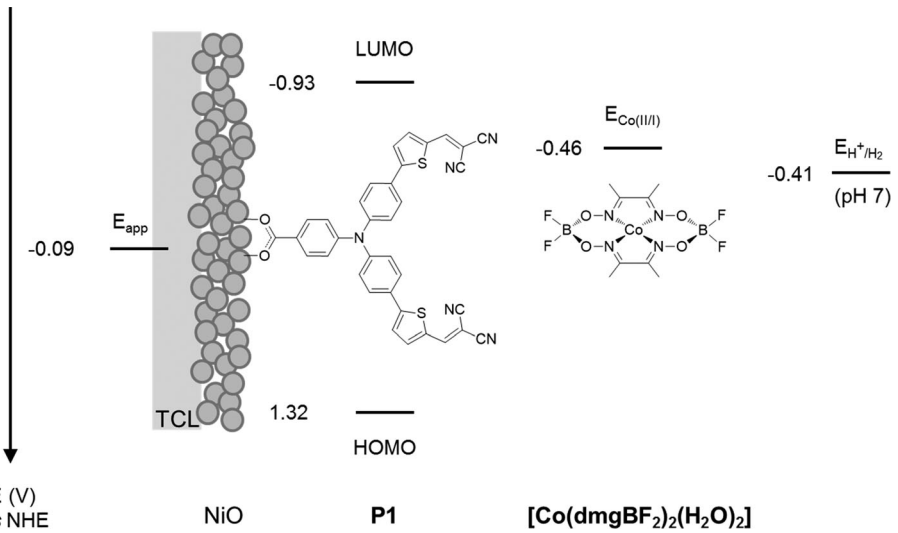

Fig. 2 Energy diagram of NiO-**P1**-$[Co(dmgBF_2)_2(H_2O)_2]$ electrodes (note: potentials of **P1** in MeCN from Qin *et al.*[16] and for $[Co(dmgBF_2)_2(H_2O)_2]$ in pH 7 phosphate buffer corrected *vs.* NHE from Berben *et al.*[20]). TCL: transparent conducting layer.

the reduced dye (−0.93 V *vs.* NHE)[16] is sufficient to reduce I_3^- to I^- or $[Co(dmgBF_2)_2(H_2O)_2]$ both from the Co(II) to the Co(I) state, the entry point of the catalytic proton reduction cycle, and further from the Co(III)–H to form the active Co(II)–H species.[17–19]

Experimental

Sample preparation

Sample **1a**/**1b** was prepared by following the method according to Grätzel for TiO_2.[21]

Sample **2** was prepared by grinding 3 g of NiO ground in planetary mill (500 rpm) for 24 h with EtOH. 10 mL of ethyl cellulose 10% in EtOH, 20 mL terpineol were added and the EtOH was removed under vacuum. The paste was deposited onto FTO glass by screen printing. The electrodes were sintered according to the following program:

Sample **3** was prepared according to Bräutigam *et al.*[22] Minor alterations included the deposition by doctor blading and the 3-fold repetition of this to yield thicker NiO surfaces.

Sample **4** conducting glass substrates were cut to size and then cleaned in an ultrasonic bath for 15 minutes, first in soapy water, second in propan-2-ol and finally in acetone. The NiO precursor solution was prepared by dissolving anhydrous $NiCl_2$ (1 g) and the tri-block co-polymer F108 (poly(ethylene glycol)-*block*-poly(propylene glycol)-*block*-poly(ethylene glycol)) (1 g) in ethanol (6 g) and ultrapure Milli-Q water (5 g).[23] NiO electrodes were made by applying the precursor solution onto conducting glass substrates (Pilkington TEC15, sheet resistance 15 Ω sq^{-1}) by doctor blade using Scotch tape as a spacer (0.2 cm^2 active area), followed by sintering in a Nabertherm B150 oven at 450 °C for 30 min.

Samples **5a–d** were purchased from Dyenamo, where they are prepared by screen printing (one layer for sample **a** and **b** and two layers for samples **c** and **d**). The as-received plates were sintered in a flat oven (PZ28-3TD, Harry Gestigkeit) monitored by a controller (Programmer PR5, Detlef Gestigkeit) applying the following temperature gradients:

– For samples **a** and **c**: from r.t. to 350 °C in 30 min; 30 min at 350 °C; gently back to r.t.

– For samples **b** and **d**: from r.t. to 450 °C in 30 min; 30 min at 450 °C; gently back to r.t.

Samples **5e,f** were prepared by Solaronix by screen printing of a NiO paste (Ni-Noxide N/SP). The as-received plates were sintered in a flat oven (PZ28-3TD, Harry Gestigkeit) monitored by a controller (Programmer PR5, Detlef Gestigkeit) applying the following temperature gradients:

– For samples **e**: from r.t. to 350 °C in 30 min; 30 min at 350 °C; gently back to r.t.

– For samples **f**: from r.t. to 450 °C in 30 min; 30 min at 450 °C; gently back to r.t.

Samples **6a–c** were prepared according to D'Amario *et al.*[24] 3 g of anhydrous $NiCl_2$ and 3 g of F108 polymer were dissolved in a mixture of deionized water (9 g) and 99.5% ethanol (18 g). The resulting green viscous solution was sonicated overnight. The mixture was centrifuged for 15 min to sediment out undissolved $NiCl_2$ and amorphous NiO. After centrifugation, the supernatant was collected as four separate batches for use as doctor-blading paste. The Li-doping was carried out by adding 0, 0.1 and 0.5 mol% of LiCl to the $NiCl_2$ sol–gel. The LiCl was added by water solution using less than 1% of the final batch volume. Then, the mixture was stirred for 1 day. Mesoporous NiO electrodes were prepared by spreading the doctor-blading paste onto FTO glass masked with adhesive tape and sintered in a furnace at 450 °C for 30 min.

Table 1 Sintering gradient used for preparation of sample 2

	Start temperature (°C)	End temperature (°C)	Ramp	Time at fixed temperature
1	RT	110	30 min	30 min
2	110	250	1 h	30 min
3	250	340	15 min	5 min
4	340	400	30 min	30 min

Sample **7** commercial NiO nanoparticles (1.0 g, 20 nm Inframat Advanced Materials) were mixed with of ethanol (8.0 mL), acetic acid (0.2 mL), terpinol (3.0 g) and ethyl cellulose (0.5 g) by ball-milling for 2 h. The obtained paste was screen-printed on clean FTO glass, followed by sintering at 450 °C in air for 30 min (Table 2).

Electron microscopy

SEM micrographs for **5e** and **f** were recorded using a FEI Quanta200 3D DualBeam FIB/SEM. High resolution TEM was recorded using the JEOL 2100F TEM equipped with a JEOL digital STEM system and a Gatan Tridiem spectrometer at the Nottingham Nanoscience and Nanotechnology Centre. The NiO was removed from the FTO glass and loaded onto a carbon coated copper TEM grid (Agar Scientific).

Powder X-ray diffraction (PXRD)

PXRD patterns were collected at room temperature in the 10°–80° range on a PANanalytical Multi-purpose Diffractometer operated at 40 kV and 40 mA (Cu Kα1, λ = 1.5406 Å). Powder samples were deposited from a slurry in ethanol onto a silicon zero diffraction plate and NiO films on FTO were prepared as described above. The data was analysed using PANanalytical X'Pert Highscore.

Kr gas adsorption isotherms

Adsorption isotherms were carried out by using a Micromeritics ASAP 2420 (Micromeritics, Norcross, GA, USA) using krypton as the adsorbate. NiO samples were prepared as described above onto *ca.* 0.5 cm × 1 cm FTO glass substrates. Three replicates of each sample were inserted into glass sample tubes with a sealed frit. The samples were degassed under vacuum at 25 °C for 3 hours to remove moisture and other adsorbed gases. Krypton isotherms were acquired from 0.07–0.25 relative pressure (p/p_0) at −195.85 °C in liquid nitrogen (N_2). The glass samples were then weighed and reweighed following the removal of the NiO in order to give an accurate sample weight. The BET model for specific surface area was fitted to the Kr isotherms using Microactive V3.0 software (Micrometrics Instrument Corporation).

Table 2 A summary of the samples used in this study

Sample	Deposition	Area (cm^2)	Type	Sintering		Thickness (μm)
				Ramp	Final	
1a	Screen print	0.25	Aldrich nanoparticles (around 20 nm)	40 min ramp r.t. to 550 °C	30 min@550 °C	2[b]
1b		0.25	Aldrich nanoparticles (around 20 nm)	40 min ramp r.t. to 550 °C	30 min@550 °C	5[b]
2	Screen print	0.36	Inframat nanoparticles (around 20 nm)	(See Table 1)		1.4[a]
3	Doctor blade 3 layers	0.36	Copolymer PS-b-P2VP		30 min@450 °C	0.2[a]
4	Doctor blade	0.20	F108	30 min ramp r.t. to 450 °C	30 min@450 °C	0.83[b]
5a	Screen print 1 layer	0.46	Dyenamo	30 min ramp r.t. to 350 °C	30 min@350 °C	0.74[a]
5b		0.44		30 min ramp r.t. to 450 °C	30 min@450 °C	
5c	Screen print 2 layers	0.37		30 min ramp r.t. to 350 °C	30 min@350 °C	1.75[a]
5d		0.26		30 min ramp r.t. to 450 °C	30 min@450 °C	
5e	Screen print 1 layer	0.41	Solaronix	30 min ramp r.t. to 350 °C	30 min@350 °C	
5f		0.37		30 min ramp r.t. to 450 °C	30 min@450 °C	
6a	Doctor blade	0.25	0% Li-doped F108		30 min@450 °C	0.70 ± 0.05[b]
6b			0.1% Li-doped F108			
6c			0.5% Li-doped F108			
7	Screen print 1 layer		Inframat nanoparticles (around 20 nm)		30 min@450 °C	

[a] Measured from SEM cross sectional images. [b] Measured using a Dektak Profilometer.

Electrochemistry

Cyclic voltammetry was carried out using a Palmsens Emstat potentiostat. A three electrode system was used with the NiO film working electrode, a Ag/Ag^+ (Sat. AgCl in 3 M $NaCl_{(aq)}$) reference electrode and a Pt wire counter electrode immersed in pH 7 buffer solution.

Solar cells

The NiO electrodes were soaked in an acetonitrile solution of **P1** (0.3 mM) for 16 h at room temperature. The dyed NiO electrode was assembled face-to-face with a platinized counter electrode (Pilkington TEC8, sheet resistance 8 Ω sq^{-1}) using a 30 μm thick thermoplastic frame (Surlyn 1702). Then the electrolyte, containing LiI (1.0 M) and I_2 (0.1 M) in acetonitrile, was introduced through the pre-drilled hole in the counter electrode, which was sealed afterwards. The UV-visible absorption spectra of the dyes adsorbed on NiO films were recorded using an Ocean Optics USB2000 + VIS-NIR fibre-optic spectrophotometer. Current–voltage measurements were measured using an Ivium CompactStat potentiostat under AM1.5 simulated sunlight from an Oriel 150 W solar simulator, giving light with an intensity of 100 mW cm^{-2}. Incident photon-to-current conversion efficiency curves (IPCE) were recorded by passing the light from the solar simulator through an Oriel Cornerstone 130 1/8m monochromator and recording the current from the solar cell with an Ivium CompactStat potentiostat which was calibrated against a Si photodiode.

Small amplitude square wave modulated (SSWM) photovoltage and photocurrent experiments were performed on the same p-DSCs used for the *J–V* and IPCE measurements at open circuit and short circuit, respectively. SSWM experiments were carried out over a range of light intensities, using an Ivium Modulight as a modulated light source with a 10% modulation of light intensity. The photovoltage and photocurrent rise and decays were recorded using an Ivium CompactStat potentiostat, the lifetimes were fitted to a 1st order exponential decay using Origin Pro 8. Charge extraction was performed using the same equipment, the cell was illuminated at open-circuit until a constant V_{OC} was reached, the light source was then switched off allowing for a decay in photovoltage, over a range of time intervals. Following this the cell was switched to short-circuit conditions and the current decay over 10 seconds was integrated to give the charge at varying photovoltages.

Photoelectrochemical measurements

For the electrochemical measurements a custom-built three compartment cell was used. A Pt wire (0.5 mm) counter electrode and a Ag/AgCl reference electrode were employed. The working electrode for each experiment were typically prepared on TEC 15 FTO glass with areas ranging between 0.636–0.25 cm^2. The sample preparation for each electrode was identical: (1) the NiO films were soaked in a CH_3CN dye bath containing **P1** (0.3 mM) for a period of 12 h. (2) The films were rinsed in CH_3CN to remove unadsorbed dye. (3) Finally, the co-catalyst $[Co^{II}(dmg\text{-}BF_2)_2(OH)_2]$ was introduced by slow drop-casting 100 μL of a 2 mM solution in CH_3CN and the sample was dried in air.

The electrolyte used in all experiments was an aqueous solution containing 50 mM phosphate at pH 7. All solutions were degassed by bubbling with Ar for a minimum of 5 minutes prior to commencing of the experiment and Ar was continually bubbled through the solution using a Bronkhorst flow-controller (flow rate = 10 mL min^{-1}) throughout the measurement. A 200 μL sample of the Ar flowing out from the cell was analyzed automatically every 3 min using a gas chromatograph (Shimadzu 2014) with a thermal conductivity detector operating at 50 °C. There was insufficient H_2 produced in the cell to quantify it accurately using this method. The visible LED used for photolysis is an OSRAM® OSTAR® white LED with an output of 1000 lm. Care was taken to place the LED in an identical position for

each measurement. A constant potential of −0.4 V *vs.* Ag/AgCl was applied during each experiment and the current measured using an EmStat potentiostat.

Results and discussion

Film morphology

All the NiO samples were based on nanoparticles prepared either *in situ* or pre formed and applied as a paste using a combination of organic surfactants and binders. Full details are given in the Experimental section and the corresponding references. In general the particle shape and film morphology was similar for each sample. SEM for **1** can be found in ref. 34. SEM images for samples **2** and **5b** and **d** are provided in Fig. 3. High resolution TEM for **5e–f** are shown in Fig. 4. SEM images for the sol–gel prepared films **3**, **4** and **6** have previously been reported in ref. 12, 20 and 22 respectively and high resolution TEM images for **4** are provided in Fig. 4.

Powder X-ray diffraction (PXRD)

The undyed NiO films were characterised using powder X-ray diffraction both for the samples on FTO and for the nanoparticles removed from the glass substrate. A representative X-ray diffraction pattern for the film on FTO (Fig. 5a) and the powder removed from the film (Fig. 5b) are given below.

The results of the XRD analysis are summarised in Table 3 for the film and powder respectively. The mean crystallite size estimated from the major diffractions ranged from 10 to 20 nm. Generally as the sintering temperature increases the mean crystallite size also increases, with the smallest being 10 nm for **5e** corresponding to a sintering temperature of 350 °C while the larger samples of 16 (**1a**) and 21 nm (**4**) were sintered at 550 and 450 °C respectively. For the screen printed pastes (**7**, **5d**, **1a**) sintered at 450 °C the mean crystallite sizes were fairly consistent and within the range of 13–16 nm while generally the NiO films made *via* a sol–gel process (**6**, **3**) were within the range of 12–14 nm which is smaller than for the screen printed pastes. The difference in crystallite size for the two films made *via* a sol–gel process using F108 (21 nm for the undoped film, **4**, to 12 nm with 0.5% Li, **6**) are attributed to the different solvent ratio in the precursor solution. The crystallite size in the Li-doped film **6** is in agreement with previously reported results by Sumikura *et al.* (12 nm with F108) and a slightly larger crystallite size was reported by Li *et al.* (16 nm).[12,23] Differences of around 1 nm were observed when comparing the mean crystallite size of the NiO films on FTO and the nanoparticles removed from the glass substrate. However, rather than a change in morphology this has been attributed to improved resolution for the measurement on the silicon zero diffraction plate (Fig. 5b) compared to the NiO on FTO (Fig. 5a) where there is a significant overlap of the diffractions from NiO and SnO_2.

This is most apparent for the thinner films (see ESI†) where the NiO diffractions were very low in intensity compared to those from SnO_2. Interestingly the crystallite size for samples **1**, **2** and **7** prepared from commercial NiO was less than the advertised average particle size of 20 nm. Samples **2** and **7**, which both contain Inframant NiO, agreed within 1 nm.

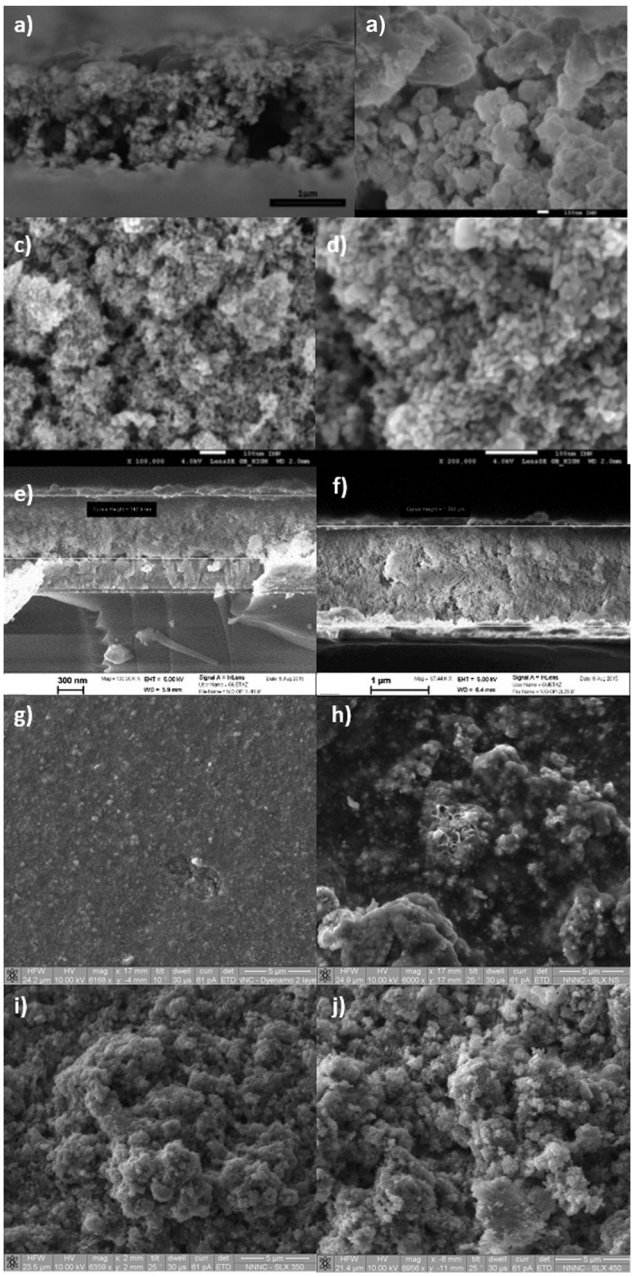

Fig. 3 SEM micrographs of (a), (b) the cross-section of **2** (50 000× magnification); (c) the surface morphology of **2** (100 000×), (d) the surface morphology of **2** (200 000×), (e) the cross section of **5b** (100 000×); (f) the cross section of **5d** (67 000×); (g) the surface of **5b** (6000×); (h) the surface of a film made from the Solaronix paste before sintering (6000×); (i) the surface of **5e** (6000×); (j) the surface of **5f** (7000×). HV = 5 kV (for sample **2**), 4 kV (**5b**, **5d**) 10 kV (**5e**, **5f**). WD = 2–5 mm.

Kr gas adsorption

A summary of the surface areas obtained from Kr adsorption isotherms is given in Table 3 and examples of adsorption isotherms for samples **5c** and **5d**, as well as **3** and **4**, respectively, are given in Fig. 6. All samples gave BET surfaces areas within

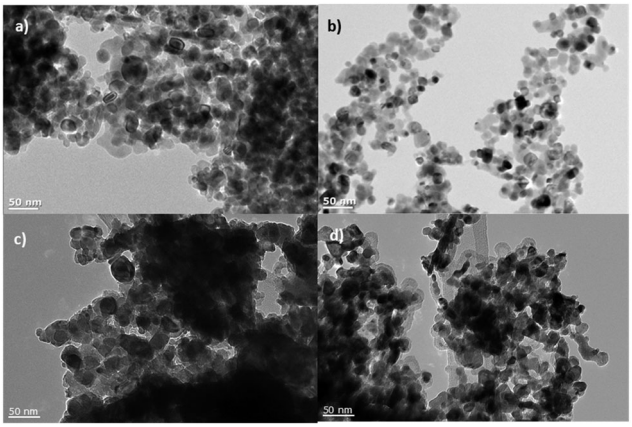

Fig. 4 High resolution TEM micrographs of (a) **1**, (b) 4, (c) **5e** and (d) **5f** at 50 000× magnification.

Table 3 Summary of the textural characterisation for NiO samples **1–7**

Sample	BET surface area[a] (m^2 g^{-1})	Mean crystallite size[b,c] (nm)
1	21.46 ± 0.07	16.1
2	—	(14.0)
3	7.71 ± 0.45	13
4	40.56 ± 0.19	20.6 (19.7)
5a	41.79 ± 0.71	(17)
5c	39.36 ± 0.77	—
5d	70.92 ± 0.58	15.4
5e	63.15 ± 0.46	9.9
6a	24.46 ± 0.70	—
6b	31.28 ± 0.44	—
6c	22.17 ± 0.54	11.5
7	60.48 ± 0.17	13.7 (14.8)

[a] BET specific surface areas obtained from Krypton adsorption isotherms. [b] Average mean crystallite size for NiO films on FTO, calculated using the Scherrer equation. [c] In parentheses, average mean crystallite size for NiO nanoparticles.

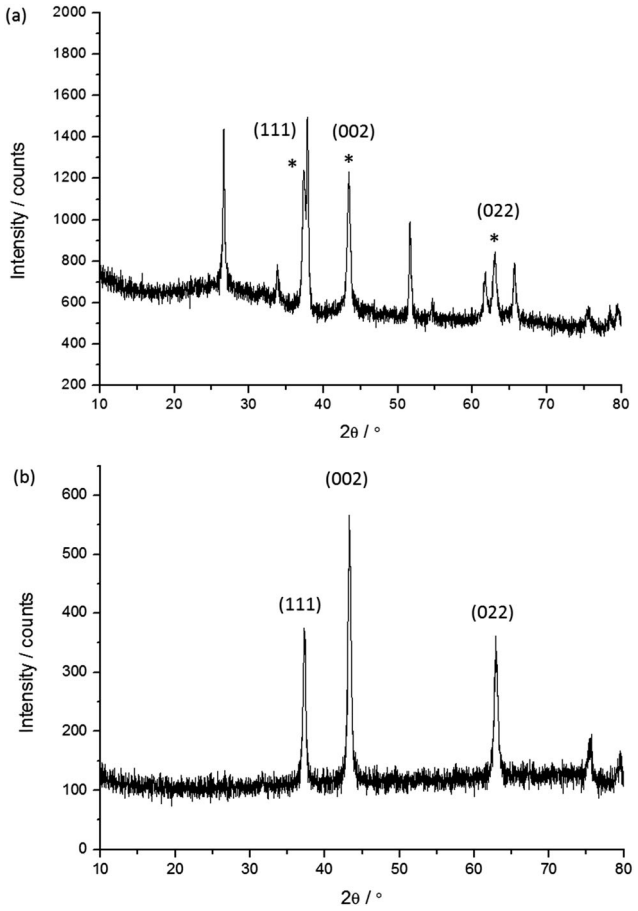

Fig. 5 Representative X-ray diffraction patterns for sample **4**: (a) the NiO film on FTO; (b) the NiO nanoparticles removed from the film. The diffraction peaks indexed with the (*hkl*) notation correspond to the main NiO phase.[25] * Denotes the peaks corresponding to NiO.

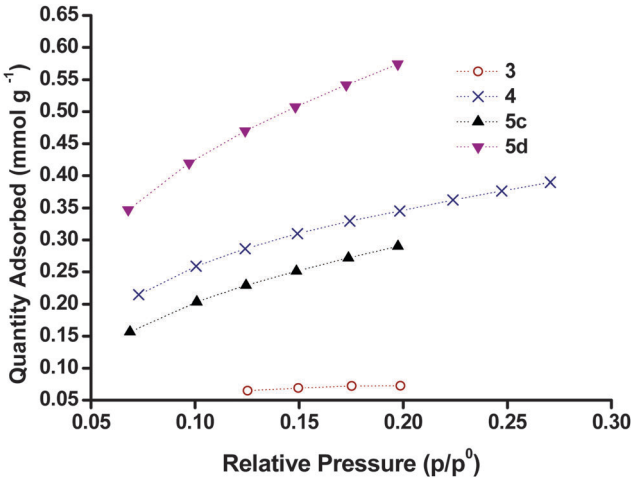

Fig. 6 Kr gas adsorption for NiO films made from NiO films made from sol–gel methods with different block copolymers, **4** (blue) and **3** (brown) and Dyenamo NiO paste and sintered at 350 °C (**5c**, black) and 450 °C (**5d**, purple).

an order of magnitude (7–70 m^2 g^{-1}). NiO screen printing pastes Dyenamo (**5d**), Solaronix (**5e**), typically had the highest surface areas (60–70 m^2 g^{-1}). There was a significant difference in the surface areas obtained from the NiO films with commercial NiO nanoparticles, **1b** (Sigma Aldrich) and 7 (Inframat). The highest surface area was obtained with **5d** which was prepared from the Dyenamo NiO paste and sintered at 450 °C (71 m^2 g^{-1}). As shown in Fig. 6, this was significantly higher than the surface area obtained for **5c** sintered at 350 °C (39 m^2 g^{-1}) and it demonstrates the importance of temperature on the formation of NiO films. Here we attribute the lower surface area for the film sintered at lower temperature to incomplete combustion of the organic binders. However, sample **5e** made from the Solaronix screen printing paste and sintered 350 °C had a comparatively high surface area (63 m^2 g^{-1}). Unfortunately it was not possible to acquire gas adsorption for this paste sintered at 450 °C. In sol–gel NiO films, higher temperature are required to ensure the all the polymer template has been removed.[23] A study by Bach *et al.* demonstrated that sintering at higher temperatures (550 °C) improves the crystallinity but can lead to a large drop in the surface area (122 m^2 g^{-1} for unsintered NiO, 56 m^2 g^{-1} for 10 minutes at 550 °C and 12 m^2 g^{-1} for 200 minutes at 550 °C).[26] This may

explain the difference between samples **1b** and 7 made from commercial nanoparticles.

Also shown in Fig. 6 is the Kr adsorption for samples **3** and **4** which were prepared by sol–gel routes. The surface areas for the samples prepared from sol–gel methods were generally lower than those obtained from pre-formed NiO nanoparticles. The BET surface area of **4** was in agreement with the N_2 BET for NiO prepared by the same method reported by Sumikura *et al.*[23] However, the sample **6a**, which was prepared from the same method had a significantly lower surface area (24 m^2 g^{-1}). The sol–gel samples prepared using a polystyrene-*block*-poly(2-vinylpyridine) diblock copolymer template (**3**) gave the lowest surface area (7.7 m^2 g^{-1}). This value was significantly lower than the values for this sample using N_2 as the adsorbate as reported previously by Bräutigam *et al.* (*ca.* 50 m^2 g^{-1}).[22] Yet, we note that the preparation method for these samples has been slightly altered from the literature (*cf.* experimental part).

Cyclic voltammetry

Cyclic voltammetry (CV) was performed in a 50 mM phosphate buffer electrolyte at pH 7 with a scan rate of 20 mV s^{-1}. Two characteristic broad but distinct peaks can be observed in the anodic and cathodic scans for all the NiO electrodes including the Li-doped NiO sample **6b**. The peak current density and peak area in the voltammograms of the six NiO films shown in Fig. 7 differed greatly. The peak current density for both processes (and area under the peaks) was highest for the screen-printed NiO films **5d** and 7 (150–200 μA cm^{-2}), while **1b** and **3** exhibited very low redox peaks (less than 50 μA cm^{-2}). As a higher specific surface area leads to more active sites exposed to the electrolyte where electron transfer can take place, the magnitude of the peak area should be related to the specific surface area of the film. The results from the cyclic voltammetry were in agreement with the BET surface area (*vide supra*), for example, **5a** and 7 have the highest BET surface, while the surface area of **1b** and **3** were much lower. The matching trend in increasing peak area with increasing surface area is consistent with redox chemistry occurring at the surface of the electrodes.[27]

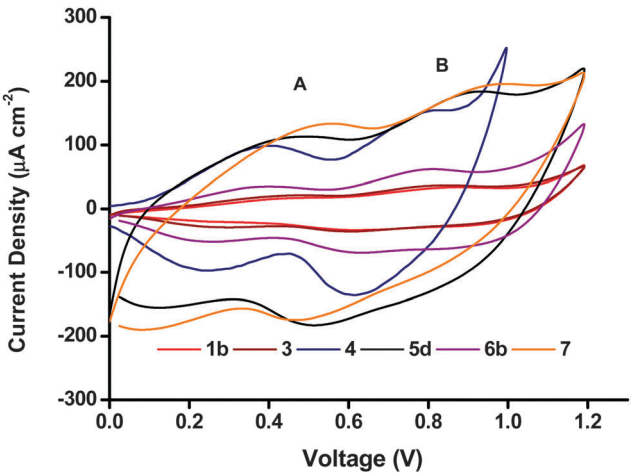

Fig. 7 Cyclic voltammograms of the different NiO preparations, recorded in phosphate buffer (0.05 M pH 7) at a scan rate of 20 mV s^{-1}.

The two peaks have previously been attributed to Ni^{2+}/Ni^{3+} (peak A) and Ni^{3+}/Ni^{4+} (peak B), respectively.[11] However, if all the Ni atoms were first oxidized to Ni^{3+}, and then to Ni^{4+}, peak A and peak B should have a similar area.[27] In Fig. 7, the area of peak B seems to be consistently larger than the area of peak A. It could suggest that remaining Ni^{2+} might be directly oxidized to Ni^{4+} in peak B. Yet, we note the comparison of peak area for A and B is challenging due to the capacitive underlying currents. The overall attribution of the electrochemical processes is thus more complicated and probably does not involve the complete oxidation of all surface sites of NiO. This discussion falls out of the scope of the current manuscript but an analysis is available in ref. 11 and 28.

Dye-sensitized solar cells

IPCE, and APCE measurements. The NiO electrodes were sensitized with the **P1** dye, first reported by Qin *et al.* which produces one of the highest reported IPCE in NiO dye-sensitized solar cells.[12,29] The UV-visible absorption spectra of the sensitized films in addition to the IPCE and Absorbed Photon-to-Current Efficiency (APCE) p-type DSCs assembled with **5d** are summarized in Fig. S2 (ESI†) as an example. The data for all films are provided in Fig. 8 and Table 4.

There was a large difference in the optical density of the non-dyed NiO samples, which ranged between 0.16 (**6a**, **1a**) to 2.9 (7) at 500 nm. The films with the highest optical density were opaque and appear almost black. The optical density of all films increased upon sensitization with **P1**. This additional increase in optical density was most pronounced at 500 nm, *i.e.* at the maximum of the dye absorption.

Difference absorption spectra of the dye on the NiO surface were obtained *via* subtraction of the absorption spectra of the non-dyed NiO films from the spectra of the dye-sensitized NiO. We attribute the brown color of the films to the presence of Ni^{3+}

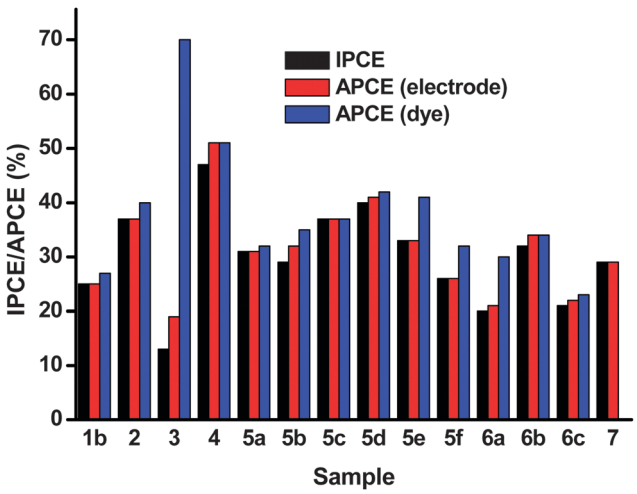

Fig. 8 Summary of all IPCE measurements and the derived APCE at 500 nm. The filled (first) bar indicates the IPCE value, the red bar (second) indicates the APCE calculated from the absorption spectrum of the complete electrode, and the blue (third) shows the APCE calculated from the difference dye spectrum of the surface.

Table 4 Summary of the IPCE values, APCE values relative to the absorption of the dye-sensitized NiO electrode, and APCE values relative to the difference absorption of the dye on the NiO films at 500 nm

Sample	IPCE (%)	APCE, electrode (%)	APCE, dye (%)	Absorbance at 500 nm (a.u.)
1b	25	25	27	3.17
2	37	37	40	2.33
3	13	19	70	0.51
4	47	51	51	1.12
5a	31	31	32	1.78
5b	29	32	35	1.05
5c	37	37	37	3.33
5d	40	41	42	1.98
5e	33	33	41	2.89
5f	26	26	32	3.23
6a	20	21	30	1.23
6b	32	34	34	1.64
6c	21	22	23	1.37
7	29	29	—	1.94

rather than Ni^0 since no Ni^0 was observed in the XRD patterns.[25,27] APCE spectra were calculated with respect to the absorption spectra of the dye-sensitized NiO surfaces and the difference absorption spectra. These two quantities should allow for the differentiation of photons absorbed by the electrode and photons absorbed only by the dye on the surface. The APCE is related to the dye on the NiO surface and reduces the wavelength dependency of the efficiency. However, for the samples in which the NiO itself absorbed strongly, the APCE values were disproportionately high (Table 4). This was particularly evident for sample **7** which had the highest absorption of all the NiO films tested making the calculation of an APCE from the dye on the surface inaccurate. Likewise sample **3** had the highest APCE using this method but the lowest IPCE because it had the smallest absorption from the dye. Some of the color from the NiO is bleached on dye adsorption which can introduce an error. Also some samples scatter light more than others. We obtained the most consistent results by calculating the APCE from the total absorbance of the film, without subtracting the spectrum for the non-sensitized NiO.

The results of the IPCE and APCE measurements are provided in Fig. 8 and Table 4. The lowest IPCE values were obtained for the polystyrene-*block*-poly-(2-vinylpyridine)-templated NiO films, **3**, while highest IPCEs were attained using the F108 templated NiO, **4**. The IPCEs for the PS-*b*-P2VP templated NiO films (**3**) were low due to the relatively small NiO thickness of about 200 nm compared to about 1.2 μm for **4**. This translates into a lower absorbance of the film (0.5 for **3** compared to 1.12 for **4**) which limits the light harvesting efficiency (LHE)§ to 69% for **3** compared to 92% for **4**. Sample **3** also had the lowest specific surface area which would lead to lower dye-loading compared to the other samples.

In general, the highest IPCE was observed for samples **7**, **5c–e**, **2** and **4**, which were prepared by screen printing a paste containing pre-formed NiO nanoparticles except for **4** which was prepared using the sol–gel method. These samples had the highest specific surface area measured using BET and the highest current density in the cyclic voltammetry experiment. The NiO crystallite sizes ranged between 14–20 nm and samples **7**, **5e** and **2** were prepared from commercial NiO with an average particle size of 20 nm. Therefore it appears that 20 nm is the preferred size of the NiO nanoparticles in the case of our cohort of samples. However, since we did not have a sample with a higher crystallite size, we do not know if this is optimum. Smaller particles may lead to more dense packing in the film, lowering the amount of surface exposed to the electrolyte or dye solution. It is anticipated that on increasing the crystallite size the surface area should decrease. This in turn would result in lower dye loading, a lower light harvesting efficiency and a lower photocurrent. It is interesting to note that 20 nm anatase particles are used in state-of-the-art TiO_2-based dye-sensitized solar cells with iodine electrolyte.[21,30] **1b**, **5f** and **5b** which were also prepared by screen printing a paste containing pre-formed NiO nanoparticles gave a lower IPCE than similar screen-printed materials, which was consistent with the lower specific surface area. This was possibly because the sintering temperature was higher (550 °C for **1**, 450 °C for **5f** compared with 350 °C for **5e**). In general the lower sintering temperature gave better results for one-layer films.

Current–voltage measurements. The current–voltage measurements for p-type DSCs assembled with each electrode are given in Fig. 9(a) and are summarized in Table 5.

Most devices exhibited a V_{OC} between 95 and 115 mV which is typical for p-type DSCs with I_3^-/I^- electrolyte. In general, devices obtained with pre made NiO nanoparticles have a higher V_{OC}, which is consistent with results in the literature and agrees with the trend in the charge lifetime studies (*vide infra*).[11] For example, sample **7** shows the highest measured open-circuit voltage (143 mV) in the series. Lithium doping also had a clear effect on the device photovoltaic performance. The 0.5% lithium doped NiO had a V_{OC} of 129 mV (**6c**) compared to 110 mV for the undoped sample (**6a**), this difference stems from the modification of the flat-band potential of the NiO following Li-doping.[27] For samples **5a–d** increasing the sintering temperature from 350 °C to 450 °C resulted in a lower V_{OC} whereas there was little difference in V_{OC} with sintering temperature between samples **5e,f**.

In general the trends in short-circuit photocurrent density (J_{SC}) followed the same trend at the IPCE. Lithium loading had a large effect on the photocurrent density. The current density rose from 1.67 mA cm^{-2} without lithium (**6a**) to 2.56 mA cm^{-2} (**6b**) with 0.1% lithium which is consistent with an increase in LHE from 94% for **6a** to 98% for **6b**. For commercially available Solaronix NiO paste (**5e** and **f**), the effect of sintering temperature on short circuit current density was clearly demonstrated: lower sintering temperature gives higher current density: 1.57 mA cm^{-2} for the sample annealed at 350 °C and 1.15 mA cm^{-2} with annealing at 450 °C. This is also true for the Dyenamo samples (**5c** and **d**), though to a lesser extent, despite the lower specific surface area of the film **5c**. It has been widely reported that the crystallite size of NiO nanoparticles increases when the sintering temperature is increased, subsequently leading to

§ LHE = $1–10^{-A}$ where A = absorbance.

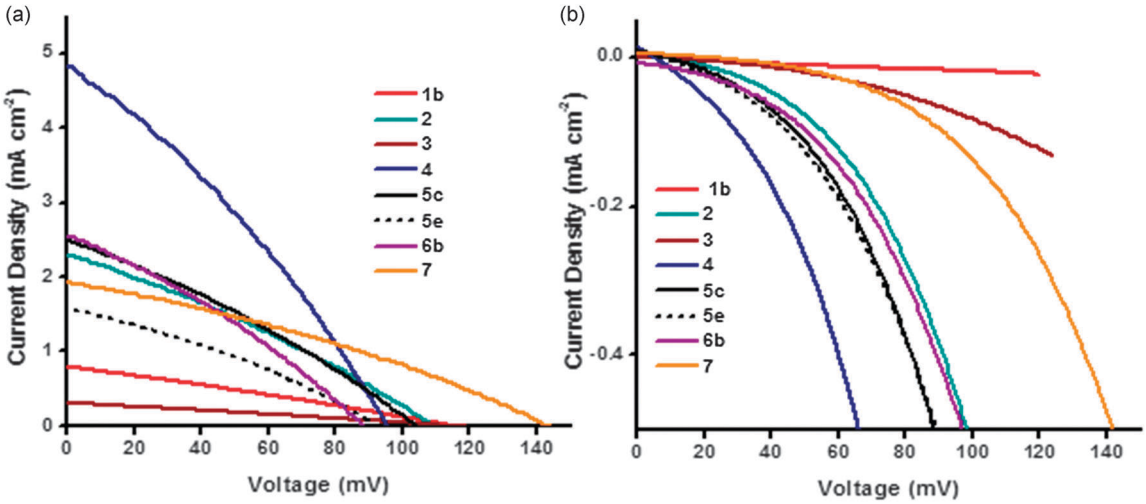

Fig. 9 Plot of current density *vs.* voltage curves (a) under AM1.5 illumination and (b) in the dark for the NiO DSCs.

Table 5 Photoelectrochemical characteristics of the p-DSCs with **P1** sensitizers employing the iodide/triiodide electrolyte recorded under AM1.5 G simulated sunlight (100 mW cm^{-2})

Sample	V_{OC} (mV)	J_{SC} (mA cm^{-2})	FF (%)	PCE (%)
1a	115	1.00	35	0.040
1b	114	0.79	28	0.025
2	110	2.31	30	0.075
3	115	0.31	26	0.009
4	96	4.83	31	0.145
5a	100	1.65	33	0.053
5b	80	1.85	29	0.042
5c	104	2.49	30	0.078
5d	98	2.40	29	0.069
5e	93	1.57	32	0.047
5f	97	1.15	32	0.035
6a	110	1.67	34	0.062
6b	88	2.56	31	0.070
6c	129	1.16	35	0.053
7	143	1.93	32	0.089

pore collapsing and a decrease in the amount of adsorbed dye and LHE.[11,31,32] Our BET measurements were inconsistent with this; **5c** had a specific surface area of 39 m^2 g^{-1} compared to 71 m^2 g^{-1} for **5d**, which suggests that 30 minutes at 350 °C is insufficient to remove all the organic material in the commercial paste. Yet, surprisingly, **5c** generated a better J_{SC}. The thickness of the films has an equally crucial effect. Following the same sintering conditions, the dye loading was greater for thicker NiO films (*e.g.* **5b** and **5d**), which is consistent with results in the literature.[12]

PS-*b*-P2VP templated sol–gel NiO films **3** suffer from very low thicknesses (around 200 nm). In this case, the dye loading and therefore the absorbance of photo-electrode was too low to afford a high photocurrent density. However, thicker films do not necessarily result in an improvement in J_{SC}. A 5 μm thick film (**1b**) produced a lower J_{SC} (J_{SC} = 0.79 mA cm^{-2}) but similar V_{OC} to a 2 μm thick film (**1a**, J_{SC} = 1.00 mA cm^{-2}). Since the specific surface area was low it is possible that dye was not adsorbed throughout the electrode or light absorption by the NiO competes with absorption from the dye.[33] Fig. 9(b) shows the dark current curves for **1–7**. Samples **1** and **3** (the thickest and thinnest samples) displayed the lowest dark currents. The low dark current density for **1b** and **3** in the presence of the (I_3^-/I^-) redox electrolyte (Fig. 9(b)) is consistent with the low current density of **1b** and **3** in the presence of the aqueous electrolyte (Fig. 7), which suggests that the conductivity of the material is low. These observations could result from slow charge-recombination at the NiO/electrolyte interface or slow charge diffusion though the NiO, possibly as a consequence of poor connectivity in the mesoporous structure, and also may explain the low J_{SC} and IPCE. The optimum film thickness appears to be in the range of 1–2 μm which maximizes the LHE and charge-diffusion through the NiO films. The highest J_{SC} (4.83 mA cm^{-2}) was obtained with sample **4** which generated the highest photoconversion efficiency (PCE) of 0.145%. This sample appears to have the optimal surface area and thickness (1.2 μm). These results were consistent with a **4** having the best charge collection efficiency. This was deduced from the charge-lifetimes and transport times which were determined using small amplitude modulated photovoltage and photocurrent decay techniques.

Charge lifetime and charge extraction studies

Charge lifetimes (τ_h) and extracted charge densities were measured by small square modulated photovoltage and charge extraction measurements. τ_h *vs.* open-circuit photovoltage (V_{OC}) and open-circuit extracted charge density (Q_{OC}) are given in Fig. 10. Q_{OC} as a function of V_{OC} is displayed in Fig. 11. When τ_h was plotted as a function of V_{OC}, sample **3** has a similar value as *e.g.* sample **1** and **2**, but when plotted against Q_{OC}, τ_h for **3** is shifted relative to the other samples. This is possibly a consequence of the very thin films. With the exception of **3**, τ_h appears to be longer for the samples made from preformed NiO compared to those prepared from sol–gel methods. This fits with the higher V_{OC} obtained by these devices as discussed earlier. Fig. S3 in the ESI† compares the effect sintering temperature has on τ_h for

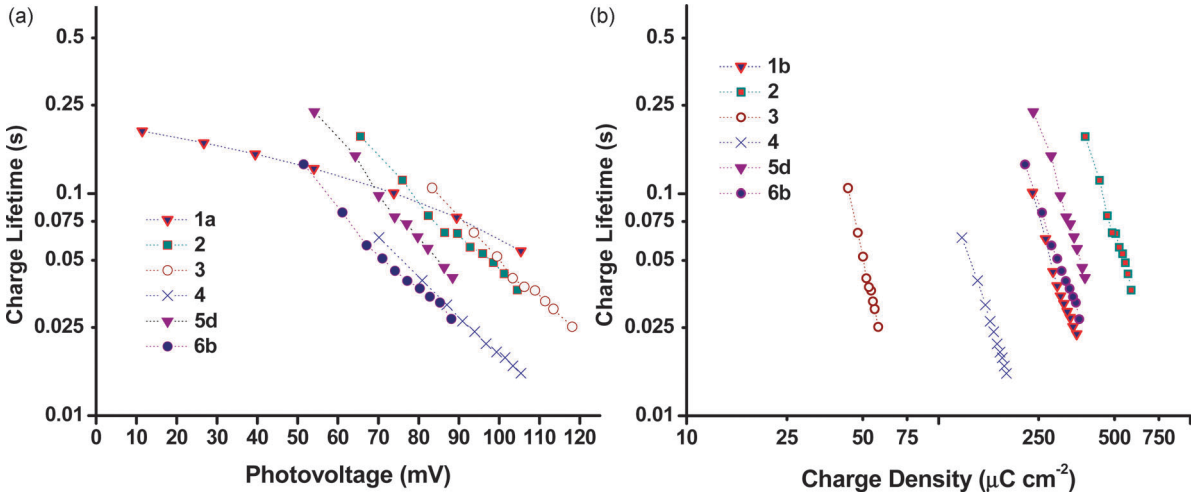

Fig. 10 Plots of charge lifetime *vs.* (a) photovoltage and (b) charge density.

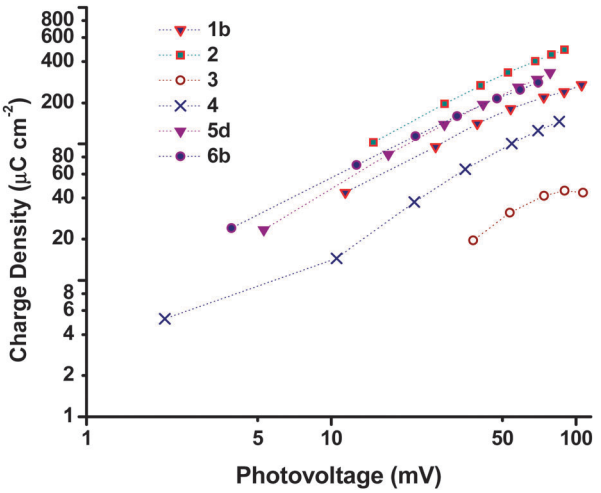

Fig. 11 Plot of extracted charge density *vs.* photovoltage.

the Dyenamo (**5c,d**) and Solaronix (**5e,f**) samples. At both sintering temperatures τ_h was longer for samples prepared from the Dyenamo NiO paste. In both cases τ_h decreased with increased sintering temperature, which is consistent with the decrease in V_{OC}. Also in both cases there seems to be a drop in Q_{OC} as a function of V_{OC} with increased sintering temperature. This implies a shift in the valence band edge which explains the higher V_{OC} obtained by sample **5f** compared to sample **5e** despite the notably shorter τ_h. Of the samples prepared from preformed NiO, **1b** had the shortest τ_h. **1b** was sintered at 550 °C, notably higher than any other samples in this study. This is somewhat unexpected as higher sintering temperatures have been used to obtain highly crystalline NiO or to post-treat samples, and has previously led to improved V_{OC}.[31,32]

τ_h and Q_{OC} for the Li doped samples **6a–c** as well as sample **4** are given in Fig. S4 (ESI†). The level of Li doping appears to have a notable effect on both τ_h and the potential of the valence band edge resulting in a significant improvement of 19 mV passing from undoped **6a** to 0.5% doped **6c**. Interestingly sample **4** which was prepared using the same F108 block copolymer as **6a** had different τ_h and Q_{OC} at similar values of V_{OC} whereas the p-DSC containing **4** had a lower overall V_{OC} at 1 sun compared to **6a**. As discussed above, we attribute the different properties to the different solvent ratio in the sol–gel precursor.

Photoelectrochemical experiments

The NiO samples were used as photocathodes in water-splitting DSPEC cells as described in the study by Li *et al.* and the photoelectrocatalytic proton reduction properties were compared.[13] As for the DSCs, the sintered NiO electrodes were first sensitized with the organic dye **P1** (Fig. 2). After rinsing the electrodes to remove unabsorbed dye, the $[Co(dmgBF_2)_2(H_2O)_2]$ H_2-evolving catalyst solution was drop-cast onto the surface of these electrodes to give a total loading of *ca.* 200 nmol cm^{-2}.¶ The catalyst-**P1** co-sensitized electrodes were then allowed to dry in air before they were assembled in the cell and immersed in aqueous pH 7 phosphate buffer. The photocurrent was recorded at an applied potential of −0.4 V *vs.* Ag/AgCl (*i.e.* −0.19 V *vs.* NHE, +0.22 *vs.* RHE) under chopped white LED illumination. The results are shown in Fig. 12. The stabilized photocurrents in the range of 5–25 μA cm^{-2} indicate electron-transfer from the photosensitized electrodes to the bound catalyst. All electrodes display an initially high transient current, rapidly decreasing to steady values. This phenomenon is particularly true for the first two irradiation periods (2 × 5 min), and tends to disappear for the last ones. This transient current may be attributed to capacitive charging of the NiO substrates or to the reduction of residual oxygen in the media. It was not observed during the whole measurement time and no anodic transient current, accounting for a back-electron-transfer, was observed when the light was switched off.

The photocurrent generated by each sample was similar in magnitude (*ca.* 10 μA cm^{-2}). The three NiO samples which produced the highest performances were **4**, **5d** and **7**, within the

¶ Accounting for the area of the substrate not the specific surface area of the sample.

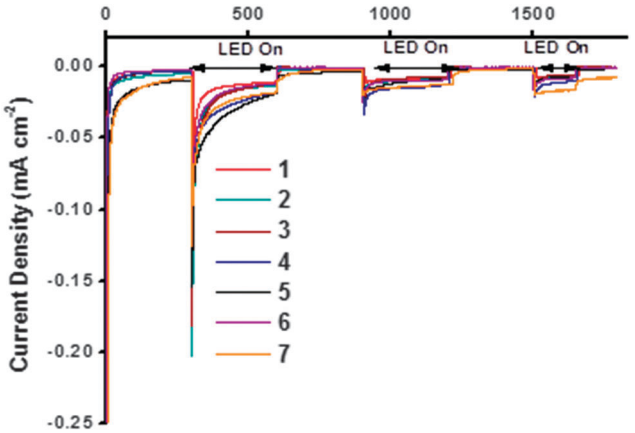

Fig. 12 Summary of water-splitting data. The maximum photocurrent reported by Li *et al.* = 5.5 μA cm^{-2}.[13]

Table 6 Summary of water-splitting data

Sample	Area (cm^2)	Total charge LED on[a] (mC)	Theoretical H_2[a] (nmol)
1b	0.25	1.97	10.2
2	0.30	3.35	17.4
3	0.36	6.56	34.0
4	0.36	9.57	49.6
5d	0.36	9.42	48.8
6b	0.36	6.7	34.7
7	0.36	9.71	50.3
Li *et al.*[13]	1.0		93 nmol after 30 min

[a] After 800 seconds.

accuracy of the measurements. These electrodes had the highest specific surface area according to the BET experiments and cyclic voltammetry (*vide supra*). **4** (purple line) generated a photocurrent starting from 25 μA cm^{-2} and slowly decreasing to 12 μA cm^{-2} after 20 minutes. The total charge under irradiation corresponds to a theoretical amount of 49.6 nmol of H_2 after 800 seconds. A similar behavior was observed on electrode **5d**, which generated the highest initial photocurrent but this decayed more steeply than the other samples to values below 10 μA cm^{-2}. Sample 7 generated the steadiest current under irradiation, stabilizing at around 20 μA cm^{-2}. This corresponded to the highest theoretical amount of evolved hydrogen (50.3 nmol). It was noted that the expected H_2 production performances of these three samples were within a very close range and exceeded that reported by Li *et al.* after correction for surface area (Table 6).[13]

Conclusions

From these studies it appears that a crystallite size of at least 20 nm, a film thickness of 1–2 μm and a specific surface area above 40 m^2 g^{-1} is most appropriate for photoelectrochemical devices using NiO. For thinner films, a lower sintering temperature (350 °C) gave better results than a higher sintering temperature (450 °C and 500 °C). Both commercial and non-commercial NiO gave promising solar cell and water-splitting devices. There was a generally higher specific surface area for preformed NiO nanoparticles compared to NiO formed *in situ* which was consistent with the trends in current density and charge in the cyclic voltammetry experiments. All the NiO films from different preparation methods showed typical electrochemical behaviour in redox electrolyte and phosphate buffer, but the differences in charge transferred varied consistently in agreement with the specific surface area of the electrode. This is a consequence of the surface confinement of the oxidation process in NiO thin film electrodes.

Samples **4** and 7 which had the two highest PCEs (0.145% and 0.089%) in the p-DSCs also gave the best overall theoretical H_2 conversion. However, the current voltage data for these two samples differed; sample **4** generated the highest photocurrent; sample 7 generated a relatively poor current but the V_{OC} for the DSC was the highest in this study. It appears that taking measures to improve both the current generated (surface area, hole mobility) and voltage across the device (surface passivation, tuned valence band energy) in a p-DSC are both key-approaches to improve dye sensitized photocathodes for hydrogen photoelectrochemical production.

Acknowledgements

We thank COST Action CM1202, The Leverhulme Trust (RPG-2013-090), The University of Nottingham, the Swedish Energy Agency, the French National Research Agency (Labex program, ARCANE, ANR-11-LABX-0003-01) and the FCH Joint Undertaking (ArtipHyction Project, Grant Agreement no. 303435) for funding.

References

1 J. He, H. Lindström, A. Hagfeldt and S. Lindquist, *J. Phys. Chem. B*, 1999, **103**, 8940–8943.
2 J. He, H. Lindström, A. Hagfeldt and S. Lindquist, *Sol. Energy Mater. Sol. Cells*, 2000, **62**, 265–273.
3 W. Song, Z. Chen, C. R. K. Glasson, K. Hanson, H. Luo, M. R. Norris, D. L. Ashford, J. J. Concepcion, M. K. Brennaman and T. J. Meyer, *ChemPhysChem*, 2012, **13**, 2882–2890.
4 E. S. Andreiadis, M. Chavarot-Kerlidou, M. Fontecave and V. Artero, *Photochem. Photobiol.*, 2011, 946–964.
5 N. Queyriaux, R. T. Jane, J. Massin, V. Artero and M. Chavarot-Kerlidou, *Coord. Chem. Rev.*, 2015, **304–305**, 3–19.
6 A. Nattestad, A. J. Mozer, M. K. R. Fischer, Y.-B. Cheng, A. Mishra, P. Bäuerle and U. Bach, *Nat. Mater.*, 2010, **9**, 31–35.
7 S. Mathew, A. Yella, P. Gao, R. Humphry-Baker, B. F. E. Curchod, N. Ashari-Astani, I. Tavernelli, U. Rothlisberger, M. K. Nazeeruddin and M. Grätzel, *Nat. Chem.*, 2014, **6**, 242–247.
8 Y. Gao, X. Ding, J. Liu, L. Wang, Z. Lu, L. Li and L. Sun, *J. Am. Chem. Soc.*, 2013, **135**, 4219–4222.
9 L. Tong, A. Iwase, A. Nattestad, U. Bach, M. Weidelener, G. Götz, A. Mishra, P. Bäuerle, R. Amal, G. G. Wallace and A. J. Mozer, *Energy Environ. Sci.*, 2012, **5**, 9472.

10 Z. Li, W. Luo, M. Zhang, J. Feng and Z. Zou, *Energy Environ. Sci.*, 2013, **6**, 347–370.
11 D. Dini, Y. Halpin, J. G. Vos and E. A. Gibson, *Coord. Chem. Rev.*, 2015, **304–305**, 179–201.
12 L. Li, E. A. Gibson, P. Qin, G. Boschloo, M. Gorlov, A. Hagfeldt and L. Sun, *Adv. Mater.*, 2010, **22**, 1759–1762.
13 L. Li, L. Duan, F. Wen, C. Li, M. Wang, A. Hagfeldt and L. Sun, *Chem. Commun.*, 2012, **48**, 988–990.
14 C. J. Wood, G. H. Summers and E. A. Gibson, *Chem. Commun.*, 2015, **51**, 3915–3918.
15 C. Baffert, V. Artero and M. Fontecave, *Inorg. Chem.*, 2007, **46**, 1817–1824.
16 P. Qin, J. Wiberg, E. A. Gibson, M. Linder, L. Li, T. Brinck, A. Hagfeldt, B. Albinsson and L. Sun, *J. Phys. Chem. C*, 2010, **114**, 4738–4748.
17 J. T. Muckerman and E. Fujita, *Chem. Commun.*, 2011, **47**, 12456.
18 B. H. Solis and S. Hammes-Schiffer, *J. Am. Chem. Soc.*, 2011, **133**, 19036–19039.
19 T. Lazarides, T. McCormick, P. Du, G. Luo, B. Lindley and R. Eisenberg, *J. Am. Chem. Soc.*, 2009, **131**, 9192–9194.
20 L. A. Berben and J. C. Peters, *Chem. Commun.*, 2010, **46**, 398–400.
21 S. Ito, P. Chen, P. Comte, M. K. Nazeeruddin, P. Liska, P. Péchy and M. Grätzel, *Prog. Photovoltaics Res. Appl.*, 2007, **15**, 603–612.
22 M. Bräutigam, P. Weyell, T. Rudolph, J. Dellith, S. Krieck, H. Schmalz, F. H. Schacher and B. Dietzek, *J. Mater. Chem. A*, 2014, **2**, 6158.
23 S. Sumikura, S. Mori, S. Shimizu, H. Usami and E. Suzuki, *J. Photochem. Photobiol., A*, 2008, **199**, 1–7.
24 L. D. Amario, G. Boschloo, A. Hagfeldt and L. Hammarström, *J. Phys. Chem. C*, 2014, **118**, 19556–19564.
25 A. Renaud, B. Chavillon, L. Cario, L. Le Pleux, N. Szuwarski, Y. Pellegrin, E. Blart, E. Gautron, F. Odobel and S. Jobic, *J. Phys. Chem. C*, 2013, **117**, 22478–22483.
26 A. Nattestad, M. Ferguson, R. Kerr, Y.-B. Cheng and U. Bach, *Nanotechnology*, 2008, **19**, 295304.
27 G. Boschloo and A. Hagfeldt, *J. Phys. Chem. B*, 2001, **105**, 3039–3044.
28 A. G. Marrani, V. Novelli, S. Sheehan, D. P. Dowling and D. Dini, *ACS Appl. Mater. Interfaces*, 2014, **6**, 143–152.
29 P. Qin, H. Zhu, T. Edvinsson, G. Boschloo, A. Hagfeldt and L. Sun, *J. Am. Chem. Soc.*, 2008, **130**, 8570–8571.
30 A. Hagfeldt, G. Boschloo, L. Sun, L. Kloo and H. Pettersson, *Chem. Rev.*, 2010, **110**, 6595–6663.
31 X. L. Zhang, F. Huang, A. Nattestad, K. Wang, D. Fu, A. Mishra, P. Bäuerle, U. Bach and Y.-B. Cheng, *Chem. Commun.*, 2011, **47**, 4808–4810.
32 X. L. Zhang, Z. Zhang, D. Chen, P. Bäuerle, U. Bach and Y.-B. Cheng, *Chem. Commun.*, 2012, **48**, 9885.
33 E. A. Gibson, M. Awais, D. Dini, D. P. Dowling, M. T. Pryce, J. G. Vos, G. Boschloo and A. Hagfeldt, *Phys. Chem. Chem. Phys.*, 2013, **15**, 2411–2420.
34 G. Naponiello, I. Venditti, V. Zardetto, D. Saccone, A. Di Carlo, I. Fratoddi, C. Barolo and D. Dini, *Appl. Surf. Sci.*, 2015, **356**, 911–920.